

JGR Solid Earth

RESEARCH ARTICLE

10.1029/2024JB030704

Key Points:

- Thermal conductivity of hydrous aluminous post-stishovite and calcium ferrite-type phase at high pressures and temperatures have been measured
- The thermal conductivity of a subducted wet basaltic crust is lower than previously modeled by ~15% at the lowermost mantle
- Hydrous, less thermally conductive slabs bring more water to deeper mantle and affect regional seismic and thermochemical structures

Supporting Information:

Supporting Information may be found in the online version of this article.

Correspondence to:

W.-P. Hsieh,
wphsieh@earth.sinica.edu.tw

Citation:

Hsieh, W.-P., Ishii, T., Deschamps, F., Tsao, Y.-C., Chang, J.-W., & Criniti, G. (2025). Reduced thermal conductivity of hydrous aluminous silica and calcium ferrite-type phase promote water transportation to Earth's deep mantle. *Journal of Geophysical Research: Solid Earth*, 130, e2024JB030704. <https://doi.org/10.1029/2024JB030704>

Received 4 NOV 2024

Accepted 12 JAN 2025

Author Contributions:

Conceptualization: Wen-Pin Hsieh

Data curation: Wen-Pin Hsieh

Formal analysis: Wen-Pin Hsieh, Takayuki Ishii, Giacomo Criniti

Funding acquisition: Wen-Pin Hsieh, Takayuki Ishii

Investigation: Wen-Pin Hsieh, Takayuki Ishii, Yi-Chi Tsao, Jen-Wei Chang

Methodology: Wen-Pin Hsieh

Project administration: Wen-Pin Hsieh

Resources: Wen-Pin Hsieh, Takayuki Ishii

Supervision: Wen-Pin Hsieh

© 2025 The Author(s).

This is an open access article under the terms of the [Creative Commons Attribution-NonCommercial License](https://creativecommons.org/licenses/by-nc/4.0/), which permits use, distribution and reproduction in any medium, provided the original work is properly cited and is not used for commercial purposes.

Reduced Thermal Conductivity of Hydrous Aluminous Silica and Calcium Ferrite-Type Phase Promote Water Transportation to Earth's Deep Mantle

Wen-Pin Hsieh^{1,2}, Takayuki Ishii³, Frédéric Deschamps¹, Yi-Chi Tsao¹, Jen-Wei Chang¹, and Giacomo Criniti⁴

¹Institute of Earth Sciences, Academia Sinica, Taipei, Taiwan, ²Department of Geosciences, National Taiwan University, Taipei, Taiwan, ³Institute for Planetary Materials, Okayama University, Misasa, Japan, ⁴Earth and Planets Laboratory, Carnegie Institution for Science, Washington, DC, USA

Abstract Subduction of oceanic slabs introduces chemical heterogeneities in the Earth's interior, which could further induce thermal, seismic, and geodynamical anomalies. Thermal conductivity of slab minerals crucially controls the thermal evolution and dynamics of the subducted slab and ambient mantle, while such an important transport property remains poorly constrained. Here we have precisely measured high pressure-temperature thermal conductivity of hydrous aluminous post-stishovite ($\Lambda_{\text{Hy-Al-pSt}}$) and aluminum-rich calcium ferrite-type phase (Λ_{CF}), two important minerals in the subducted basaltic crust in the lower mantle. Compared to the dry aluminous stishovite and pure stishovite, hydration substantially reduces the $\Lambda_{\text{Hy-Al-pSt}}$, resulting in ~9.7–13.3 W m⁻¹ K⁻¹ throughout the lower mantle. Surprisingly, the Λ_{CF} remains at ~3–3.8 W m⁻¹ K⁻¹ in the lower mantle, few-folds lower than previously assumed. Our data modeling offers better constraints on the thermal conductivity of the subducted oceanic crust from mantle transition zone to the lowermost mantle region, which is less thermally conductive than previously modeled. Our findings suggest that if the post-stishovite carries large amounts of water to the lower mantle, the poorer heat conduction through the basaltic crust reduces the slab's temperature, which not only allows the slab bringing more hydrous minerals to greater depth, but also increases slab's density and viscosity, potentially impacting the stability of heterogeneous structures at the lowermost mantle.

Plain Language Summary Earth's surface water could be transported into the deep interior via slab subduction, forming the downgoing process of deep water cycle that affects the nature and evolution of the mantle. Knowledge of the thermal transport property of slab minerals along subduction is essential, since it would significantly advance our understanding of slab's subduction dynamics and mantle's thermochemical evolution. Here, we precisely determine the thermal conductivity of hydrous aluminous post-stishovite and aluminum-rich calcium ferrite-type phase in a lower-mantle basaltic lithology along a representative geotherm of a sinking slab. We find that when incorporated with large amounts of water, the subducted slab would be cooler than previously modeled, due to the less thermally conductive oceanic crust. This would make the deep interior more hydrated and could influence seismic structures and thermochemical evolution in the deep lower mantle.

1. Introduction

Through slab subduction, seawater can be infiltrated into subducted oceanic slabs, resulting in the hydration of rock-forming minerals in the basaltic crust and lithosphere. The presence of water in the Earth's interior substantially impacts its geophysical, geochemical, and geodynamical properties (e.g., Hirschmann & Kohlstedt, 2012; Muir & Brodholt, 2018; Ohtani, 2020 and references therein). Mineral physics studies have shown that most of the major constituting minerals in the pyrolitic upper and lower mantle could only accommodate up to ~0.1 wt% water (nominally anhydrous) in their crystal structures, except for wadsleyite and ringwoodite in the mantle transition zone, which could store ~1–3 wt% water (Peslier et al., 2017). By contrast, water-bearing (hydrous) minerals in a subducted slab, for example, dense hydrous magnesium silicates (DHMSs) that undergo a series of phase transitions during subduction, typically can hold ~few to 10 (or more) wt% water, but they could only survive under relatively low temperature conditions within the slab (Ohtani, 2020). Once these hydrous minerals are broken down due to sufficiently high temperature conditions, water would be released to the surrounding crustal materials and mantle, whose physical, chemical, and rheological properties could in turn be

Writing – original draft: Wen-Pin Hsieh, Takayuki Ishii, Frédéric Deschamps
Writing – review & editing: Wen-Pin Hsieh, Takayuki Ishii, Frédéric Deschamps, Yi-Chi Tsao, Jen-Wei Chang, Giacomo Criniti

altered, leading to, for example, earthquakes in the slab (Chien et al., 2024; Kim et al., 2023) and partial melts in the ambient mantle with lower density, seismic velocity, and viscosity, etc (Ohtani, 2020; Ohtani & Ishii, 2024).

In addition to the DHMSs, basaltic crustal materials not only could play similarly important roles in carrying water to the deep interior, but also affect regional seismological (e.g., seismic scatterers) and geodynamical (e.g., slab stagnation) features around the subducted slab (see (Goes et al., 2017; Hsieh, Marzotto, Tsao, et al., 2022; Kaminsky, 2017) and reference therein). Compared to the pyrolytic mantle, the mid-ocean ridge basalt (MORB) that forms the subducted basaltic crust has higher concentrations of SiO_2 , Al_2O_3 , and Na_2O , etc. High pressure-temperature (P - T) mineral phase equilibrium experiments indicated that the MORB subducted to the upper mantle conditions is primarily made of garnet along with small, variable fractions of clinopyroxene and SiO_2 silica (Ishii et al., 2019). As subducted to the lower mantle conditions, the MORB is typically made of SiO_2 stishovite (~20 vol%), Al-rich calcium ferrite (CF)-type phase and/or new hexagonal aluminous (NAL) phase (~20 vol%), (Fe,Al)-bearing bridgmanite (FeAl-Bm, ~40 vol%), and davemaoite (~20 vol%) (Hirose et al., 2005; Ishii et al., 2019; Ono et al., 2001; Ricolleau et al., 2010). Among them, SiO_2 stishovite is of particular interest and its physical properties have been extensively explored (e.g., Andraut et al., 1998; Bolfan-Casanova et al., 2009; Hirose et al., 2005; Lakshtanov et al., 2007; Litasov et al., 2007; Yang & Wu, 2014; Zhang et al., 2022). Importantly, previous studies have suggested that the SiO_2 could contain small amounts of water, for example, less than ~0.3 wt%, depending on its Al content (Lakshtanov et al., 2007; Litasov et al., 2007). Recently the water storage capacity and stability of SiO_2 under relevant lower mantle high P - T conditions have been an important, but debated topic. For instance, (Lin et al., 2020, 2022; Nisr et al., 2020) suggested that pure SiO_2 could hold large amounts of water (>3 wt%) even at lower mantle's high P - T conditions. However, very recently (Purevjav et al., 2024; Takaichi et al., 2024) showed that the water solubility in pure SiO_2 drops at higher temperatures in their experiments, leading to a contradictorily limited water storage capacity. Moreover (Ishii, Criniti, et al., 2022), investigated the stability and water solubility of aluminous SiO_2 stishovite and its high-pressure polymorph, CaCl_2 -type post-stishovite at the top lower mantle conditions. They found that the aluminous SiO_2 can store up to ~1.1 wt% water, since the solubility of Al_2O_3 and water in SiO_2 increase with temperature. Such a unique feature allows the aluminous SiO_2 to transport more water to deep mantle through slab subduction with higher P - T conditions.

Thermal conductivity of slab minerals is of fundamental importance, as it critically controls the heat flux and thermal evolution of a subducted slab. The thermal profile in turn influences the stability zone, phase transition and dehydration depth, and water solubility of minerals in the subducted crust and lithosphere, as well as the subduction dynamics of the slab. Recently, (Hsieh, Marzotto, Tsao, et al., 2022) showed that both pure and Al_2O_3 -bearing dry stishovite's thermal conductivity are fairly high, which cause fast warming of a sinking slab, promoting slab stagnation and crust detachment at the shallow lower mantle. However, these measurements were performed on dry minerals and the effects of water on the thermal conductivity of SiO_2 and subducted MORB assemblage along a slab's geotherm has never been investigated.

In addition to the SiO_2 , Al-rich phases (including the CF phase and NAL) that could contain ~40 wt% Al_2O_3 (Ricolleau et al., 2010) are also major constituents of the MORB when subducted to the lower mantle. Prior studies have shown that depending on their compositions, typically the NAL only co-exists with the CF phase until ~40–50 GPa (Ono et al., 2009; Ricolleau et al., 2010 and references therein), after which the NAL disappears and the CF phase becomes the dominant Al-rich phase below the mid-lower mantle. Though several physical properties of the CF phase with different compositions have been intensively explored (e.g., Dubrovinsky et al., 2002; Ono et al., 2009; Ricolleau et al., 2010; Tutti et al., 2000; Wang et al., 2020; Wu et al., 2017; Yin et al., 2016; Zhao et al., 2018), its thermal conductivity, like hydrous aluminous SiO_2 , under slab's high P - T conditions has never been experimentally studied. Lack of knowledge to the thermal conductivity of hydrous aluminous SiO_2 and CF phase would lead to incomplete understanding on the thermal evolution of a sinking slab as well as its impacts on the regional seismic structure and dynamics and rheology of the slab and ambient mantle.

In this work, to better constrain the thermal conductivity of subducted MORB assemblages containing hydrous aluminous SiO_2 , we have combined an ultrafast optical pump-probe method with externally heated diamond anvil cells to precisely measure the thermal conductivity of hydrous aluminous post-stishovite and CF phase at high P - T conditions. Our present experimental results combined with data modeling are fundamentally important, indicating that as the MORB incorporated with geologically relevant amounts of Al_2O_3 and water is subducted through the mantle down to the core-mantle boundary (CMB) region, it is less thermally conductive than

previously thought. This would cause a cooler condition within the slab, enabling more hydrous minerals and water to be transported to greater depth.

2. Materials and Methods

2.1. Starting Materials and Sample Preparation

Single crystals with a size of ~ 100 – 200 μm of hydrous aluminous CaCl_2 -type stishovite (post-stishovite, pSt) were synthesized with a starting mixture of reagent-grade SiO_2 quartz and $\text{Al}(\text{OH})_3$ gibbsite with 9:1 in molar ratio using a multi-anvil-press at 24 GPa and $2,000^\circ\text{C}$ for 2 hr. The detailed synthesis procedure can be seen in (Ishii, Criniti, et al., 2022). To characterize the crystal structure, we first determined the lattice parameters of these crystals as $a = 4.2358(5)$ \AA , $b = 4.1877(4)$ \AA , $c = 2.6789(4)$ \AA , and $V = 47.519(9)$ \AA^3 using a Huber diffractometer equipped with $\text{MoK}\alpha$ radiation and a point detector driven by the software SINGLE (Angel & Finger, 2011), suggesting the crystal structure is CaCl_2 -type at ambient conditions (Ishii, Criniti, et al., 2022). For water content characterization, crystals were oriented parallel to the (100) and (010) crystallographic planes, respectively, using the diffractometer and then double-side polished to 8 and 11 μm thick for polarized Fourier transform infrared (FT-IR) spectroscopy. Polarized FT-IR spectra were collected using a Bruker IFS 120 high-resolution spectrometer with a Bruker IR microscope (Supplementary Figure S1 in Supporting Information S1). The water content was calculated from spectra collected in the three mutually orthogonal directions [100] [010], and [001] using the calibration of (Paterson, 1982). Details of the water content calculation were described in (Ishii, Criniti, et al., 2022). The main components of SiO_2 and Al_2O_3 were determined using several randomly selected crystals by electron probe microanalyzer (EPMA), where standard materials of quartz (SiO_2) and synthetic corundum (Al_2O_3) were used for Si and Al, respectively. The chemical composition was characterized as $\text{Si}_{0.918(2)}\text{Al}_{0.082(2)}\text{O}_{1.982}\text{H}_{0.046(7)}$, that is, 92.85 (60) wt% SiO_2 with 6.99 (13) wt% Al_2O_3 and 0.69 (10) wt% H_2O in combination with results of FT-IR measurements. The synthesis in Ishii, Criniti, et al. (2022) operated at a slightly lower temperature of $1,900^\circ\text{C}$ and formed a homogeneously distributed water content among several randomly selected crystals. Although the water content here was examined using the limited number of crystals, given the higher synthesizing temperature in the present study, the compositional homogeneity in our samples would be even better.

As for single-crystalline CF phase samples with a crystal size of ~ 100 μm , they were synthesized with a starting mixture of $\text{NaAlSi}_3\text{O}_8$ nepheline, MgAl_2O_4 spinel, and Fe_3O_4 magnetite with 7:2:1 in molar ratio at 23 GPa and $2,000^\circ\text{C}$ for 2 hr using a multi-anvil-press (S7760, see Table 1 in Ishii, Criniti, et al., 2023). The crystals were oriented to (100) and (001) using single-crystal X-ray diffraction for thermal conductivity measurements. Their chemical composition was determined as $\text{Na}_{0.62(2)}\text{Mg}_{0.19(5)}\text{Fe}_{0.25(1)}\text{Al}_{1.20(3)}\text{Si}_{0.78(3)}\text{O}_4$ ($\text{Fe}^{3+}/\Sigma\text{Fe} = 34(1)\%$) by EPMA and Mössbauer spectroscopy. The composition is homogeneous through the sample based on the fact that we probed many points on the sample surface (see the typical SEM image in the Online Materials in Ishii, Criniti, et al., 2023) and obtained a consistent, averaged composition. Details of the synthesis and characterization were described in (Ishii, Criniti, et al., 2023).

To carry out thermal conductivity measurements at high pressure and room temperature, we first polished the samples of interest from the same batch of synthesized crystals to ~ 15 μm thick, and thermally evaporated ~ 90 -nm-thick Al film on the sample. We then loaded the sample and a ruby chip into a symmetric DAC with 200 μm culets and a rhenium gasket. By loading silicone oil (CAS No. 63148-62-9 from ACROS ORGANICS) as the pressure medium, we compressed the sample to a target pressure for thermal conductivity measurement. The pressure was determined by ruby fluorescence (Dewaele et al., 2004) with a typical uncertainty of $<2\%$. At $P > \sim 60$ GPa, we also measured the Raman spectrum of ruby and diamond anvil (Akahama & Kawamura, 2004), respectively, for pressure comparison, where their difference is typically <3 – 5 GPa, depending on the pressure regime. Moreover, for simultaneously high P - T thermal conductivity measurements, we employed an externally heated BX-90 DAC (EHDAC) loaded with helium as the pressure medium, providing a quasi-hydrostatic and homogeneous high T condition within the sample chamber. Since the heating-induced thermal pressure affected the total pressure on the sample, we included a gas membrane in our EHDAC to in situ manipulate the pressure, which was determined also by ruby fluorescence, yet calibrated for high temperature effect following (Datchi et al., 2007). The pressure uncertainty in high P - T measurements is $<2\%$ – 3% (Hsieh, Chang, et al., 2024).

2.2. Thermal Conductivity Measurements

We used time-domain thermoreflectance (TDTR) coupled with DAC or EHDAC to precisely measure the lattice thermal conductivity of pSt and CF phase at variable high P - T conditions up to ~ 100 GPa and 1023 K, respectively (Hsieh, Deschamps, et al., 2024; Hsieh et al., 2018; Zhou et al., 2022). In brief, in our TDTR system, we split the output of a Ti:sapphire laser into pump and probe beams. The pump beam heated up the Al film on the sample, producing time-dependent variations in optical reflectivity that was then probed by the probe beam. We collected the temporal variations in the reflected probe beam intensity that correlate with the sample's thermal conductivity using a silicon photodiode and a lock-in amplifier. Details of the TDTR principles, experimental setup coupling TDTR with symmetric DAC or EHDAC along with data and uncertainty analyses were described in (Cahill, 2004; Chien et al., 2024; Hsieh et al., 2009; Hsieh, Tsao, & Lin, 2022; Hsieh, Deschamps, et al., 2024) and references therein.

A representative TDTR spectrum for hydrous aluminous pSt at 90.3 GPa and room temperature fitted by a bi-directional thermal model is shown in Supplementary Figure S2 in Supporting Information S1. We note that in our data analysis, the Al's thickness and sample's heat capacity are two key parameters to derive the sample's thermal conductivity. We estimated the Al's thickness under high P - T conditions following a recently developed method in (Hsieh, Chang, et al., 2024), where we monitored the potential change in sample's surface area during our experiments since it would affect the Al's thickness. As for the heat capacity, though our aluminous pSt contains ~ 0.69 wt% H_2O , such amount of water is not expected to substantially alter the heat capacity from pure stishovite; we thus treated the heat capacity of hydrous aluminous pSt as that of dry aluminous stishovite (Hsieh, Marzotto, Tsao, et al., 2022). Since the heat capacity of our CF phase sample at high P - T conditions is unknown, we assumed it is similar to the $MgAl_2O_4$ (Yin et al., 2016). We emphasize that our conductivity uncertainty is majorly resulted from data analysis (uncertainties of thermal model parameters), rather than from the measurements. Using the method presented in Supplementary Figure S3 in Supporting Information S1 (Cahill & Watanabe, 2004; Zheng et al., 2007), we estimated the thermal conductivity uncertainty is $<10\%$ at $P < 30$ GPa and $\sim 10\%$ – 15% at $P = 30$ – 100 GPa.

3. Results

3.1. High-Pressure, Room-Temperature Lattice Thermal Conductivity of Hydrous Aluminous pSt and CF Phase

In Figure 1, we first present the thermal conductivity of hydrous aluminous pSt ($\Lambda_{Hy-Al-pSt}$, red solid circles with (100) orientation and black solid squares with (010) orientation) as a function of pressure to 104 GPa at room temperature. The $\Lambda_{Hy-Al-pSt}$ is ~ 22 $W m^{-1} K^{-1}$ at ambient conditions and increases upon initial compression. As the applied pressure reaches ~ 15 GPa, the $\Lambda_{Hy-Al-pSt}$ starts to decrease until ~ 22 GPa. Though at $P < 22$ GPa, the crystal structure of our pSt sample ($CaCl_2$ -type) is different from that of the essentially dry stishovite with 5 wt% Al_2O_3 (rutile-type), their thermal conductivity are comparable to each other (the thermal conductivity of dry stishovite with 5 wt% Al_2O_3 , $\Lambda_{anHy-Al-St}$, from (Hsieh, Marzotto, Tsao, et al., 2022) is plotted as the blue dashed curve in Figure 1). This suggests that the slight structural difference between rutile- and $CaCl_2$ -type and the relatively small amounts of 0.69 wt% H_2O in our pSt serving as lattice impurities play minor roles in affecting the $\Lambda_{Hy-Al-pSt}$ at $P < 22$ GPa. The decrease in the $\Lambda_{Hy-Al-pSt}$ between 15 and 22 GPa may be related to changes in transport properties in pSt (Criniti et al., 2023). studied the crystal structure and Raman spectrum of $Si_{0.886}Al_{0.114}O_{1.980}H_{0.074}$ pSt, and confirmed that the hydrous aluminous pSt remains in the $CaCl_2$ -type structure from ambient to at least 50 GPa, that is, there is no structural transition. Furthermore, they also observed that the Raman frequency of the A_g mode softens with pressure until around 16 GPa and then remains almost a constant around 20 GPa, after which it stiffens at higher pressure. They argued that such behavior may be associated with the changes in hydrogen bonding located between oxygens consisting of the $(Si,Al)O_6$ octahedra, that is, a high thermally activated hydrogen mobility due to a broad energy potential without barrier of this state, as discussed in the $CaCl_2$ -type $(Al,Fe)OOH$ (Meier et al., 2022). Such a local structural change could cause changes in transport properties such as thermal conductivity. Since we also observed similar changes in the A_g mode of our pSt around 22 GPa (Supplementary Figure S4 in Supporting Information S1), the decrease in $\Lambda_{Hy-Al-pSt}$ around 15–22 GPa may be attributed to the local structural change of pSt.

Upon further compression, the $\Lambda_{Hy-Al-pSt}$ suddenly increases from ~ 22 $W m^{-1} K^{-1}$ at 22 GPa to 27.5 $W m^{-1} K^{-1}$ at 24.5 GPa, followed by a slight decrease with pressure until ~ 37 GPa. Note that the slight reduction is within our

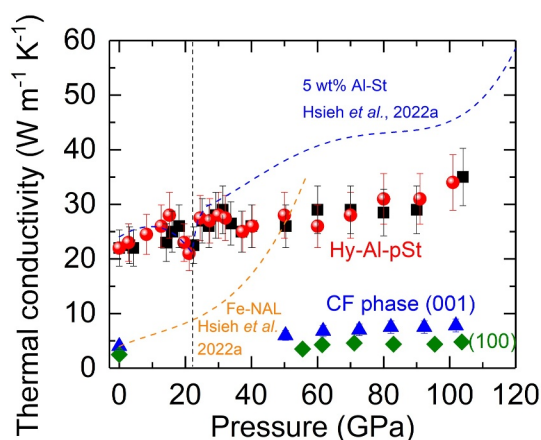


Figure 1. Lattice thermal conductivity of hydrous aluminous post-stishovite ($\Lambda_{\text{Hy-Al-pSt}}$) and CF phase (Λ_{CF}) at high pressure and room temperature. For $\Lambda_{\text{Hy-Al-pSt}}$, two separate runs of measurements (red solid circles with (100) orientation and black solid squares with (010) orientation, respectively) show consistent results to ~ 104 GPa. The $\Lambda_{\text{Hy-Al-pSt}}$ (with 6.99 wt% Al_2O_3 and 0.69 wt% H_2O) is initially comparable to that of essentially dry stishovite with 5 wt% Al_2O_3 ($\Lambda_{\text{anHy-Al-St}}$, blue dashed curve), while after ~ 22 GPa (vertical dashed line), the $\Lambda_{\text{Hy-Al-pSt}}$ progressively becomes lower than the $\Lambda_{\text{anHy-Al-St}}$. On the other hand, the Λ_{CF} along (001) (blue solid triangles) is $\sim 60\%$ higher than that along (100) (green solid diamonds) at ambient and between ~ 50 and 104 GPa; however, at $P \sim 50$ GPa both are much lower than the Fe-NAL (orange dashed curve). The error bars indicate uncertainty of data analysis. For CF phase samples, their error bars are comparable to the symbol size.

comparable to that of Fe-bearing NAL ($\Lambda_{\text{Fe-NAL}}$, orange dashed curve in Figure 1 taken from (Hsieh, Marzotto, Tsao, et al., 2022)), although their chemical compositions are different. However, at 50 GPa both the $\Lambda_{\text{CF}(001)}$ and $\Lambda_{\text{CF}(100)}$ keep such low conductivity, while the $\Lambda_{\text{Fe-NAL}}$ becomes $\sim 4\text{--}7$ times higher. In addition, it's worthy to note that (Wu et al., 2017) observed a pressure-induced spin transition of octahedral ferric ions in an Fe-bearing CF phase ($\text{Na}_{0.88}\text{Al}_{0.99}\text{Fe}_{0.13}\text{Si}_{0.94}\text{O}_4$) at $\sim 25\text{--}35$ GPa. Nevertheless, based on the structural analysis on our present Fe-bearing CF phase sample, which is almost identical to the compositions of CF phase in a MORB lithology (e.g., Ishii et al., 2019; Ishii, Chanyshv, & Katsura, 2022). (Ishii, Criniti, et al., 2023) reported that not all the ferric ions are in octahedral coordination. This result indicates that if present, a spin transition of ferric ions in octahedral sites at lower mantle pressures has limited effects on its elastic and transport properties.

3.2. Lattice Thermal Conductivity of Hydrous Aluminous pSt and CF Phase at Simultaneously High Pressure-Temperature Conditions

To investigate how the $\Lambda_{\text{Hy-Al-pSt}}$ and Λ_{CF} change with temperature ($\Lambda(T)$) under high pressures, we further performed thermal conductivity measurements at simultaneously high P - T conditions using externally heated DACs, see Figure 2 for the results. Though our measurement temperature range only spans a factor of ~ 3.5 (from 300 to 1023 K), we have observed clear temperature dependences for $\Lambda_{\text{Hy-Al-pSt}}$ and Λ_{CF} . We quantified the $\Lambda(T)$ by assuming that the thermal conductivity can be phenomenologically modeled as $\Lambda(T) = \alpha T^n$, where α is a normalization constant. We determined the exponent n by linearly fitting the $\ln\Lambda$ - $\ln T$ plot, where n is the slope. As shown in Figure 2a, the $\Lambda_{\text{Hy-Al-pSt}}$ shows a similar temperature dependence with $n = -0.69 (\pm 0.08)$ at 26–29 GPa and $-0.66 (\pm 0.06)$ at 45–48 GPa. The n values we obtained here are in good agreement with previously assumed $n = -0.75$ for dry stishovite with 5 wt% Al_2O_3 (Hsieh, Marzotto, Tsao, et al., 2022). On the other hand, the CF phase presents considerably different temperature dependence. Assuming Λ_{CF} scales with T^m , along crystal orientation of (001), $m = -0.25 (\pm 0.08)$ at 63–68 GPa and $m = -0.3 (\pm 0.07)$ at 60–65 GPa; along crystal orientation of (100), m shows a similar value of $-0.29 (\pm 0.09)$ at 64–69 GPa. Such temperature dependence ($T^{-0.25}$ to -0.3) is much weaker than the previously assumed $T^{-0.5}$ for Fe-bearing NAL (Hsieh, Marzotto, Tsao, et al., 2022), suggesting that the complex impurity effects due to abundant, various cations in CF phase causes even stronger phonon-

data uncertainty, and its origin requires further studies to understand. Application of higher pressure enhances the $\Lambda_{\text{Hy-Al-pSt}}$ but with a smaller increasing rate than that of the essentially dry pSt with 5 wt% Al_2O_3 (blue dashed curve in Figure 1); the $\Lambda_{\text{Hy-Al-pSt}}$ raises to $35 \text{ W m}^{-1} \text{ K}^{-1}$ at 104 GPa, $\sim 25\%$ lower than the $\Lambda_{\text{anHy-Al-St}}$ at similar pressure. Such lower conductivity is presumably caused by the pressure-enhanced hydration effect, where the applied pressure increases the density of H_2O impurities, enhancing inelastic scatterings with heat-carrying phonons and thus reducing the thermal conductivity. Similar pressure-enhanced hydration effects on reducing the thermal conductivity of mantle minerals had been observed in olivine (Chang et al., 2017) and ringwoodite (Marzotto et al., 2020). In addition, the two sets of data for $\Lambda_{\text{Hy-Al-pSt}}$ (red solid circles and black solid squares) were collected from separate measurements on single-crystalline hydrous aluminous pSt with different crystal orientation ((100) and (010), respectively). The fact that the $\Lambda_{\text{Hy-Al-pSt}}$ between two measurement runs are close to each other suggests a minimal effect of crystal orientation on the $\Lambda_{\text{Hy-Al-pSt}}$.

On the other hand, the thermal conductivity of CF phase (Λ_{CF}) presents drastically different values and pressure dependence than the $\Lambda_{\text{Hy-Al-pSt}}$. The Λ_{CF} along crystal orientation of (001) ($\Lambda_{\text{CF}(001)}$, blue solid triangles in Figure 1) starts from $\sim 4 \text{ W m}^{-1} \text{ K}^{-1}$ at ambient conditions and reaches $\sim 6 \text{ W m}^{-1} \text{ K}^{-1}$ at 50.3 GPa, which further increases to $7.8 \text{ W m}^{-1} \text{ K}^{-1}$ at 102 GPa. Similarly, the Λ_{CF} along crystal orientation of (100) ($\Lambda_{\text{CF}(100)}$, green solid diamonds in Figure 1) also shows a weak pressure dependence. $\Lambda_{\text{CF}(100)}$ is $\sim 2.5 \text{ W m}^{-1} \text{ K}^{-1}$ at ambient, $3.5 \text{ W m}^{-1} \text{ K}^{-1}$ at 55.5 GPa, and increases to $4.8 \text{ W m}^{-1} \text{ K}^{-1}$ at 104 GPa, overall $\sim 40\%$ lower than the $\Lambda_{\text{CF}(001)}$ over the pressure range we studied, showing a thermal conductivity anisotropy. Importantly, at ambient conditions both the $\Lambda_{\text{CF}(001)}$ and $\Lambda_{\text{CF}(100)}$ are com-

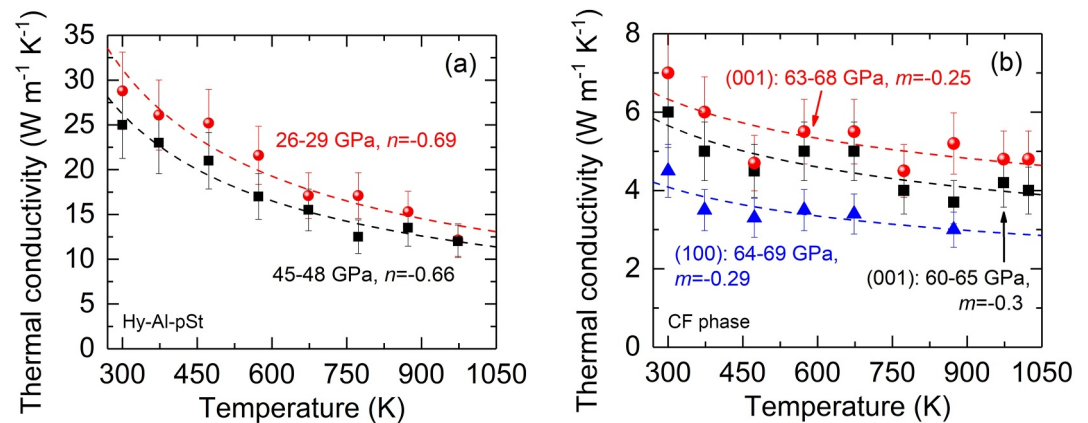


Figure 2. Temperature dependence of the thermal conductivity of (a) hydrous aluminous pSt and (b) CF phase at high pressures. Assuming the $\Lambda_{\text{Hy-Al-pSt}}$ scales with T^n , the $n = -0.69 (\pm 0.08)$ at 26–29 GPa and $-0.66 (\pm 0.06)$ at 45–48 GPa. For CF phase, the temperature exponent is $-0.25 (\pm 0.08)$ along (001) orientation at 63–68 GPa, $-0.3 (\pm 0.07)$ along (001) orientation at 60–65 GPa, and $-0.29 (\pm 0.09)$ along (100) orientation at 64–69 GPa. Dashed curves are fit to each data set for their respective temperature dependence.

impurity scatterings than those in many Fe-bearing mantle minerals with a typical $T^{-0.5}$ dependence (Chien et al., 2024; Deschamps & Hsieh, 2019; Hsieh, Marzotto, Ishii, et al., 2022; Xu et al., 2004; Zhang et al., 2019).

Note that during the high temperature measurements, the heating effect induces thermal pressure that changes the pressure within the sample chamber by a few GPa. Nevertheless, we argue that such thermally induced pressure variation does not significantly influence the temperature dependence we derived in Figure 2, because within the small range of pressure variation, the pressure has minimal effects on changing both the $\Lambda_{\text{Hy-Al-pSt}}$ and Λ_{CF} at room temperature (Figure 1). For instance, within $P = 26\text{--}29$ GPa at room temperature, the applied pressure does not substantially change the $\Lambda_{\text{Hy-Al-pSt}}$, as it remains at $\sim 27.5 \text{ W m}^{-1} \text{ K}^{-1}$ (Figure 1); thus, even though the pressure slightly varies between 26 and 29 GPa during the high T measurements (red solid circles in Figure 2a), it can be treated as an essentially constant pressure with minimal effects on the $\Lambda_{\text{Hy-Al-pSt}}(T)$. Such condition applies to all the high T measurements shown in Figure 2, allowing us to derive the exponents for their temperature dependences.

4. Discussion and Geophysical Implications

4.1. Modeling the Thermal Conductivity of Subducted Mid-Ocean Ridge Basalt Assemblage Along a Slab's Geotherm

Our results for the $\Lambda_{\text{Hy-Al-pSt}}$ and Λ_{CF} at high P - T conditions (Figures 1 and 2) enable us to better constrain the thermal conductivity profile of subducted water-bearing MORB assemblage along slab subduction. Such a profile is critical to influence the thermal evolution of a sinking slab with potential impacts on the stability of slab minerals, fate of deep water cycle, as well as geodynamics and seismic structure of the slab and ambient mantle. To model the lattice thermal conductivity of subducted water-bearing MORB assemblage (Λ_{MORB}) at relevant P - T conditions along slab subduction, for simplicity we first assumed that the MORB assemblage subducted to the depth of mantle transition zone ($\sim 410\text{--}660$ km) is composed of garnet (~ 90 vol%) and hydrous aluminous stishovite (~ 10 vol%) (Ishii et al., 2019). When subducted to the lower mantle, we assumed the MORB assemblage is composed of hydrous aluminous pSt (~ 20 vol%), Fe-NAL that transforms to CF phase at ~ 50 GPa (~ 20 vol%), FeAl-Bm (~ 40 vol%), and davemaite (~ 20 vol%) (Hirose et al., 2005; Ishii et al., 2019; Ishii, Miyajima, et al., 2022; Ono et al., 2001). Temperature and pressure dependences of the thermal conductivity for each mineral phase were either from the present study— $\Lambda_{\text{Hy-Al-pSt}}$ scales with $T^{-0.67}$ and Λ_{CF} scales with $T^{-0.28}$, or from literature results— Λ_{garnet} scales with $T^{-0.5}$ (Hung et al., 2024), $\Lambda_{\text{Hy-Al-St}}$ at $P < 22$ GPa was assumed to scale with $T^{-0.75}$ (Hsieh, Marzotto, Tsao, et al., 2022), $\Lambda_{\text{FeAl-Bm}}$ scales with $T^{-0.5}$ (Deschamps & Hsieh, 2019; Hsieh et al., 2017), $\Lambda_{\text{Fe-NAL}}$ scales with $T^{-0.5}$ (Hsieh, Marzotto, Tsao, et al., 2022), and $\Lambda_{\text{davemaite}}$ scales with $T^{-1.1}$ (Zhang et al., 2021). We then used the Voigt-Reuss-Hill (VRH) average scheme along with the volume fraction of each mineral as an estimate for the thermal conductivity of subducted water-bearing MORB

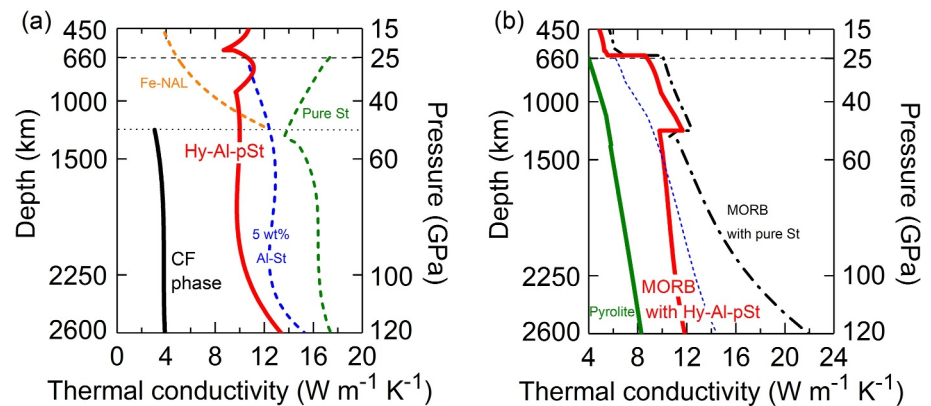


Figure 3. Modeled thermal conductivity profiles of subducted mid-ocean ridge basalt (MORB) minerals in the mantle. (a) The $\Lambda_{\text{Hy-Al-pSt}}$ (Hy-Al-pSt, red solid curve) along a representative geotherm of a subducting slab is fairly lower than the $\Lambda_{\text{anHy-Al-St}}$ (5 wt% Al-St, blue dashed curve) and $\Lambda_{\text{pure St}}$ (green dashed curve) from ~ 800 km depth to the lowermost mantle region. Once the Fe-NAL disappears at ~ 50 GPa (horizontal dotted line), leaving the CF phase as the dominant Al-rich phase in the MORB, there is a thermal conductivity drop depending on their relative volume fraction. (b) If the MORB contains hydrous aluminous St that transforms to pSt at ~ 22 GPa (red solid curve), the $\Lambda_{\text{MORB with Hy-Al-pSt}}$ is lower than that of MORB with pure stishovite (black dash-dotted curve), in particular from $\sim 1,500$ km depth all the way down to the lowermost mantle. Previously modeled Λ profiles for the pyroilite (green solid curve) and subducted MORB (blue dashed curve) taken from (Hsieh et al., 2018; Hsieh, Marzotto, Tsao, et al., 2022) are plotted for comparison.

assemblage: at transition zone depth $\Lambda_{\text{MORB}} = 0.9\Lambda_{\text{garnet}} + 0.1\Lambda_{\text{Hy-Al-St}}$, while in the lower mantle $\Lambda_{\text{MORB}} = 0.2\Lambda_{\text{Hy-Al-pSt}} + 0.2\Lambda_{\text{Fe-NAL/CF}} + 0.4\Lambda_{\text{FeAl-Bm}} + 0.2\Lambda_{\text{davemaoite}}$.

In Figure 3a, we first highlight that our modeled $\Lambda_{\text{Hy-Al-pSt}}$ and Λ_{CF} along a slab's P - T conditions in the lower mantle are both significantly lower than previously thought. Along a representative geotherm of a subducting slab that was assumed to be 800 K colder than a regular mantle geotherm (Katsura et al., 2010), the $\Lambda_{\text{Hy-Al-pSt}}$ (Hy-Al-pSt, red solid curve) becomes lower than the $\Lambda_{\text{anHy-Al-St}}$ (5 wt% Al-St, blue dashed curve, Hsieh, Marzotto, Tsao, et al., 2022) below ~ 800 km depth (~ 30 GPa), for example, lower by $\sim 20\%$ – 25% throughout the mid-lower mantle depth. Their difference is slightly reduced when the MORB is further subducted down to the lowermost mantle region. Such thermal conductivity reduction is even more pronounced (lower by $\sim 30\%$ – 40%) when compared to the conductivity of pure stishovite ($\Lambda_{\text{pure St}}$, green dashed curve, Hsieh, Marzotto, Tsao, et al., 2022) over the entire lower mantle. On the other hand, (Hsieh, Marzotto, Tsao, et al., 2022) showed that the $\Lambda_{\text{Fe-NAL}}$ (orange dashed curve in Figure 3a) reaches ~ 12.5 W m⁻¹ K⁻¹ at 50 GPa. Assuming the CF phase crystal is present with a random orientation within the subducted MORB assemblage, we here find that, by averaging $\Lambda_{\text{CF}(001)}$ and $\Lambda_{\text{CF}(100)}$, the averaged Λ_{CF} (black solid curve) is only ~ 3 W m⁻¹ K⁻¹ at 50 GPa. This suggests that the disappearance of Fe-NAL at ~ 50 GPa, leaving the CF phase as the dominant Al-rich mineral within the MORB, would induce a thermal conductivity drop that depends on the relative fraction of Fe-NAL and CF phase (e.g., drop by a factor of ~ 4.2 if the Al-rich phase is only made of Fe-NAL at $P < 50$ GPa, while only made of CF phase at $P > 50$ GPa). Note that even though the chemical composition of the Fe-NAL in (Hsieh, Marzotto, Tsao, et al., 2022) is different from that of the CF phase in the present study, such a large thermal conductivity difference cannot be fully accounted for simply by the compositional effect. As the CF phase is further subducted, the averaged Λ_{CF} slightly increases with depth, reaching ~ 3.9 W m⁻¹ K⁻¹ at the lowermost mantle region and representing the least thermally conductive phase within the subducted MORB assemblage. Interestingly, if the CF phase crystal had a preferred orientation along (100), the $\Lambda_{\text{CF}(100)}$ is only ~ 2.9 W m⁻¹ K⁻¹ at the lowermost mantle, serving as a local thermally insulating block that hinders heat transfer through the crust in the region.

Furthermore, if the stishovite within the subducted MORB contains relatively large amounts of Al₂O₃ and H₂O (e.g., ~ 7 wt% Al₂O₃ and 0.7 wt% H₂O as in our sample), our modeling shows that the $\Lambda_{\text{MORB with Hy-Al-pSt}}$ (red solid curve in Figure 3b) remains at ~ 5 W m⁻¹ K⁻¹ at the transition zone depths, while suddenly jumps to ~ 8.6 W m⁻¹ K⁻¹ as the subducted MORB is brought into the lower mantle. As the slab continues to sink down to $\sim 1,300$ km depth (~ 50 GPa), the $\Lambda_{\text{MORB with Hy-Al-pSt}}$ drops from ~ 11.6 W m⁻¹ K⁻¹ to ~ 9.7 W m⁻¹ K⁻¹ due to the disappearance of NAL and the dominant presence of CF phase. When approaching the deepest region of the

mantle, the $\Lambda_{\text{MORB with Hy-Al-pSt}}$ slightly increases to $\sim 11.8 \text{ W m}^{-1} \text{ K}^{-1}$, that is, increasing mildly by $\sim 40\%$ from the top to bottom of the mantle.

As expected, if the stishovite within the subducted MORB is pure SiO_2 that is much more thermally conductive than the dry Al-bearing and hydrous Al-bearing SiO_2 , the modeled Λ profile of such subducted MORB with pure SiO_2 ($\Lambda_{\text{MORB with pure St}}$, black dash-dotted curve in Figure 3b) is systematically higher than the $\Lambda_{\text{MORB with Hy-Al-pSt}}$ by $\sim 15\%$ at the transition zone and by $\sim 10\%$ at the shallow lower mantle until $\sim 1,300 \text{ km}$ depth. Noticeably, such difference becomes $\sim 20\%$ at mid-lower mantle and substantially increases to $\sim 85\%$ at the lowermost mantle depth, indicating a significant combined effect of water and alumina incorporations on the MORB's thermal conductivity. Moreover, in Figure 3b we also plotted the previously modeled Λ_{MORB} profile (blue thin dashed curve, Hsieh, Marzotto, Tsao, et al., 2022) for comparison, in which at that time due to the data unavailability, the Λ_{CF} was simply treated as $\Lambda_{\text{Fe-NAL}}$ by extrapolation and the $\Lambda_{\text{davemaoite}}$ was treated as $\Lambda_{\text{FeAl-Bm}}$. As such, the subducted MORB was previously assumed to be composed of dry 5 wt% Al_2O_3 -bearing stishovite with 20 vol%, Fe-NAL with 20 vol%, and FeAl-Bm with 60 vol% (i.e., the previously modeled Λ of subducted MORB = $0.2\Lambda_{\text{anHy-Al-St}} + 0.2\Lambda_{\text{Fe-NAL}} + 0.6\Lambda_{\text{FeAl-Bm}}$ throughout the entire lower mantle). We found that between 660 and $\sim 1,300 \text{ km}$ depth, our present $\Lambda_{\text{MORB with Hy-Al-pSt}}$ (red solid curve) is higher than the previously modeled profile since the thermally conductive davemaoite is now included in the present study. Below $\sim 1,500 \text{ km}$ depth, the $\Lambda_{\text{MORB with Hy-Al-pSt}}$, instead, becomes lower than the previously modeled profile, despite the inclusion of thermally conductive davemaoite. This is primarily because the $\Lambda_{\text{Hy-Al-pSt}}$ is fairly lower than $\Lambda_{\text{anHy-Al-St}}$ and the Λ_{CF} is much lower than $\Lambda_{\text{Fe-NAL}}$, as indicated in Figure 3a based on our present experimental and modeling results.

Our modelled profiles of the $\Lambda_{\text{MORB with Hy-Al-pSt}}$ and $\Lambda_{\text{MORB with pure St}}$ offer a platform to constrain and model the potential variation of the thermal conductivity of subducted MORB assemblage along slab subduction, in which, depending on the characteristics of a slab, natural stishovite could contain minimal to $\sim 6 \text{ wt}\%$ Al_2O_3 and variable amounts of water (Bolfan-Casanova et al., 2009; Ishii, Criniti, et al., 2022; Lakshtanov et al., 2007; Litasov et al., 2007). Importantly, the better constrained thermal conductivity of subducted MORB is much higher than the ambient pyrolitic mantle (green solid curve in Figure 3b, Hsieh et al., 2018), not to mentioned the conventionally assumed low constant of ~ 3 or $4 \text{ W m}^{-1} \text{ K}^{-1}$ (Davies, 1988; Eberle et al., 2002; Hofmeister, 1999; Tang et al., 2014; Wei et al., 2017).

In addition, compared to our simple assumption of the relative volume fraction of each MORB-forming mineral, different composition models had been proposed. For instance, subducted MORB may alternatively be made of $\sim 20 \text{ vol}\%$ stishovite, $\sim 30 \text{ vol}\%$ CF phase/NAL, $\sim 30 \text{ vol}\%$ FeAl-Bm, and $\sim 20 \text{ vol}\%$ davemaoite (Ishii et al., 2019). Nevertheless, the modelled Λ_{MORB} profile with such composition only minorly differs from our results of $\Lambda_{\text{MORB with Hy-Al-pSt}}$ by less than 5% throughout the entire lower mantle, smaller than our estimated uncertainty for the thermal conductivity along subduction. Yet, if there is very limited amount of NAL phase in the subducted MORB, that is, only the CF phase, rather than NAL, forms the Al-rich phase with $\sim 20\text{--}30 \text{ vol}\%$ of the MORB throughout the entire lower mantle (Ishii et al., 2019; Ishii, Miyajima, et al., 2022; Ono et al., 2001), such Λ_{MORB} profile between 660 and $\sim 1,300 \text{ km}$ depth would be $\sim 5\text{--}19\%$ lower than the $\Lambda_{\text{MORB with Hy-Al-pSt}}$. Finally, we note that the modelled Λ_{MORB} profile is insensitive to the average scheme we adopted. Using Hashin-Shtrikman scheme, the modelled Λ_{MORB} profile with the same volume fraction of each mineral phase just slightly (less than $\sim 10\text{--}15\%$) deviates from that modelled using the VRH scheme, again, a minor difference comparable to our estimated uncertainty for the thermal conductivity along subduction.

4.2. Geophysical Implications on the Thermal Evolution of a Subducting Slab and Stability of Slab Minerals

During the long journey of subduction through the mantle, the P - T conditions that the slab minerals experience play critical roles in affecting minerals' stability and thus the depth a phase transition would occur. Based on the previously modeled profile of subducted MORB (blue thin dashed curve in Figure 3b), (Hsieh, Marzotto, Tsao, et al., 2022) performed numerical simulations to investigate the thermal evolution of a sinking slab. They demonstrated that during subduction a slab's temperature profile can be significantly altered by the variation of the Λ of subducted oceanic crust due to the different MORB composition. For instance, compared to their reference case of $\Lambda_{\text{MORB}} = \Lambda_{\text{mantle}}$, depending on slab's sinking velocity, a high temperature anomaly of about tens of degree Kelvin (K) to 100–200 K can be induced, if the subducted MORB contains variable amounts of Al_2O_3 -bearing stishovite with a higher Λ than the regular mantle.

Importantly, our present profile of $\Lambda_{\text{MORB with Hy-Al-pSt}}$ is lower than the previously modeled MORB profile (blue thin dashed curve in Figure 3b) at the mantle transition zone, while becomes higher by $\sim 30\%$ between 660 and 1,500 km depth. Below a crossover at $\sim 1,500$ km depth all the way down to the lowermost mantle region, the $\Lambda_{\text{MORB with Hy-Al-pSt}}$ is less thermally conductive than the previously modeled one (by $\sim 15\%$ at the CMB). Consequently, at the transition zone depth our present $\Lambda_{\text{MORB with Hy-Al-pSt}}$ profile is expected to reduce the previously simulated high temperature anomaly within a slab, easing the potential temperature-induced instability and breakdown of DHMSs in the region (Ohtani et al., 2000), and uplifting the olivine-wadsleyite transformation depth, given a Clapeyron slope of $\sim 2.5 \text{ MPa K}^{-1}$ (Katsura & Ito, 1989).

As the slab sinks through the top region of the lower mantle, the more-thermally-conductive basaltic oceanic crust ($\Lambda_{\text{MORB with Hy-Al-pSt}} >$ previously modeled Λ_{MORB}) would enhance the high temperature anomaly at the base of the basaltic crust and top of the lithosphere. Such even warmer condition shall promote the breakdown of ringwoodite (post-spinel transition) at slightly shallower depth than 660 km depth, as its Clapeyron slope is negative and fairly small (between -0.1 and -0.9 MPa K^{-1}) (Ishii, Chanyshiev, & Katsura, 2022; Litasov et al., 2005). On the other hand, majorite and akimotoite typically break down (post-garnet and post-akimotoite transitions) at ~ 720 – 800 km depth with a Clapeyron slope of -1.5 MPa K^{-1} (Ishii, Frost, et al., 2023) and between -3.2 and -8.1 MPa K^{-1} (Chanyshiev et al., 2022), respectively. Similar to the post-spinel transition, the warmer temperature within the slab shall uplift these transitions to shallower depths, narrowing the depth gap between the post-spinel transition and post-garnet and post-akimotoite transitions at the top lower mantle. Moreover, from shallow to mid-lower mantle, due to the 30% higher MORB thermal conductivity than the previously modeled one, the even higher temperature within the subducted crust and lithosphere would reduce slab's density and viscosity, hindering slab's subduction dynamics and possibly promoting its stagnation at shallow lower mantle. Overall, depending on their composition, and in particular on their aluminum and water contents, slabs may thus sink either more, or less easily to the deep mantle, with lesser aluminum and dry slabs being more likely to be (temporally) stacked around 1,000 km depth.

If the slab sinks down to the deep lower mantle (below 1,500 km depth), the quantitative effects of our modeled $\Lambda_{\text{MORB with Hy-Al-pSt}}$ on the slab's thermal evolution and dynamics require further numerical modeling. Nevertheless, (Tsutsumi et al., 2024) recently reported that under the high P - T conditions above the CMB, the water remains stored in aluminous pSt within a subducted slab, suggesting that the hydrous aluminous pSt serves as a major water carrier to the region near the CMB. Since our modeled $\Lambda_{\text{MORB with Hy-Al-pSt}}$ is less thermally conductive than previously modeled throughout the deep lower mantle, particularly at the lowermost mantle region, the presence of hydrous aluminous pSt in the oceanic crust would prevent the slab from getting warmer, which preserves the hydrous minerals (including δ -phase and its solid solution with phase H (Ohtani, 2020), as well as pSt itself) to be transported to deeper mantle, influencing, in turn, the fate of deep water cycle. The presence of Fe-bearing δ -phase with an exceptionally low thermal conductivity (Hsieh et al., 2020) would further decrease the hydrous MORB assemblage's thermal conductivity. Moreover, it's expected that variable amounts of Al_2O_3 and water contained in the subducted MORB would alter the temperature profile within the slab and thus the depth at which hydrous minerals eventually dehydrate. This, in turn, would impact the depth and location where the partial melting of mantle aggregates occurs, leading to the formation of fairly low seismic velocity zones with low thermal conductivity (Hsieh et al., 2020), and significantly affecting the seismic and thermal structure and rheology in the region. Furthermore, (Ishii, Criniti, et al., 2022) reported that the water solubility of aluminous silica increases with temperature. As the hydrous minerals in slab's peridotite layer dehydrate, part of the released water may be stored in the aluminous pSt, which further decreases the oceanic crust's thermal conductivity, lowering the temperature within the slab. Poorly conductive and colder slabs may further impact the dynamics, structure, and heat transfer of the lowermost mantle in several ways. First, a reduced temperature within the slab would lead to a higher viscosity, which would promote interactions with the thermochemical reservoirs (such as large low velocity provinces, LLVPs), thus reducing the stability of these structures (Li et al., 2019). Second, lower temperature profile within the slab should lead to a thicker post-perovskite (pPv) layer within and around the slab. Finally, the slab temperature and thermal conductivity locally influences the CMB heat flux. Because it is colder than the average mantle, a slab is likely to induce a spike of high CMB heat flux, potentially impacting core dynamics and the geodynamo. A colder slab would of course lead to a stronger spike, but this would be partially attenuated by a poorer conductivity. Numerical simulations of mantle convection are needed to confirm and quantify these effects, providing, in turn, observational tests.

5. Conclusion

Our high P - T experimental measurements combined with data modeling show that the $\Lambda_{\text{Hy-Al-pSt}}$ and Λ_{CF} along a representative geotherm of a subducting slab are both lower than previously modeled. Our important findings significantly improve the constraints on the Λ profile of a subducted basaltic crust containing hydrous aluminous silica, which varies drastically upon phase transitions of slab minerals and is much more complex than previously thought. The two conductivity discontinuities at 660 and $\sim 1,300$ km depths would induce sudden changes in the heat flux flowing into the slab and thus its internal temperature profile. As the less thermally conductive slab containing hydrous aluminous silica is subducted down to the lowermost mantle, the reduced temperature condition promotes water transportation to greater depth. It also enhances the slab's density and viscosity, potentially impacting the stability of heterogeneous structures (e.g., LLVPs, ultralow velocity zones, pPv layer, and thermal plumes). Combinations of our present findings with future numerical modellings on the thermal evolution and dynamics of a water-bearing slab sinking through the mantle to the CMB, as well as on the interactions between the slab and ambient mantle heterogeneous structures will significantly advance our understanding of the thermochemical evolution at the lowermost mantle and fate of deep water cycle.

Conflict of Interest

The authors declare no conflicts of interest relevant to this study.

Data Availability Statement

The data used in this paper are available at (Hsieh, Ishii, et al., 2024) <https://zenodo.org/records/14002102>.

References

- Akahama, Y., & Kawamura, H. (2004). High-pressure Raman spectroscopy of diamond anvils to 250 GPa: Method for pressure determination in the multimegabar pressure range. *Journal of Applied Physics*, *96*(7), 3748–3751. <https://doi.org/10.1063/1.1778482>
- Andraut, D., Fiquet, G., Guyot, F., & Hanfland, M. (1998). Pressure-induced Landau-type transition in stishovite. *Science (New York, N.Y.)*, *282*(5389), 720–724. <https://doi.org/10.1126/science.282.5389.720>
- Angel, R. J., & Finger, L. W. (2011). Single: A program to control single-crystal diffractometers. *Journal of Applied Crystallography*, *44*(1), 247–251. <https://doi.org/10.1107/S0021889810042305>
- Bolfan-Casanova, N., Andraut, D., Amiguet, E., & Guignot, N. (2009). Equation of state and post-stishovite transformation of Al-bearing silica up to 100 GPa and 3000 K. *Physics of the Earth and Planetary Interiors*, *174*(1–4), 70–77. <https://doi.org/10.1016/j.pepi.2008.06.024>
- Cahill, D. G. (2004). Analysis of heat flow in layered structures for time-domain thermoreflectance. *Review of Scientific Instruments*, *75*(12), 5119–5122. <https://doi.org/10.1063/1.1819431>
- Cahill, D. G., & Watanabe, F. (2004). Thermal conductivity of isotopically pure and Ge-doped Si epitaxial layers from 300 to 550 K. *Physical Review B: Condensed Matter*, *70*(23), 235322. <https://doi.org/10.1103/PhysRevB.70.235322>
- Chang, Y.-Y., Hsieh, W.-P., Tan, E., & Chen, J. (2017). Hydration-reduced lattice thermal conductivity of olivine in Earth's upper mantle. *Proceedings of the National Academy of Sciences*, *114*(16), 4078–4081. <https://doi.org/10.1073/pnas.1616216114>
- Chanyshv, A., Ishii, T., Bondar, D., Bhat, S., Kim, E. J., Farla, R., et al. (2022). Depressed 660-km discontinuity caused by akimotoite–bridgmanite transition. *Nature*, *601*(7891), 69–73. <https://doi.org/10.1038/s41586-021-04157-z>
- Chien, Y. H., Marzotto, E., Tsao, Y. C., & Hsieh, W.-P. (2024). Anisotropic thermal conductivity of antigorite along slab subduction impacts seismicity of intermediate-depth earthquakes. *Nature Communications*, *15*(1), 5198. <https://doi.org/10.1038/s41467-024-49418-3>
- Crinti, G., Ishii, T., Kurnosov, A., Glazyrin, K., & Boffa Ballaran, T. (2023). High-pressure phase transition and equation of state of hydrous Al-bearing silica. *American Mineralogist*, *108*(8), 1558–1568. <https://doi.org/10.2138/am-2022-8546>
- Datchi, F., Dewaele, A., Loubeyre, P., Letoulec, R., Le Godec, Y., & Canny, B. (2007). Optical pressure sensors for high-pressure-high-temperature studies in a diamond anvil cell. *High Pressure Research*, *27*(4), 447–463. <https://doi.org/10.1080/08957950701659593>
- Davies, G. F. (1988). Ocean bathymetry and mantle convection I. Large-Scale flow and hotspots. *Journal of Geophysical Research*, *93*(B9), 10467–10480. <https://doi.org/10.1029/jb093ib09p10467>
- Deschamps, F., & Hsieh, W.-P. (2019). Lowermost mantle thermal conductivity constrained from experimental data and tomographic models. *Geophysical Journal International*, *219*(Supplement_1), S115–S136. <https://doi.org/10.1093/gji/ggz231>
- Dewaele, A., Loubeyre, P., & Mezouar, M. (2004). Equations of state of six metals above 94 GPa. *Physical Review B*, *70*(9), 094112. <https://doi.org/10.1103/PhysRevB.70.094112>
- Dubrovinsky, L. S., Dubrovinskaya, N. A., Prokopenko, V. B., & Le Bihan, T. (2002). Equation of state and crystal structure of NaAlSiO₄ with calcium-ferrite type structure in the conditions of the lower mantle. *High Pressure Research*, *22*(2), 496–499. <https://doi.org/10.1080/08957950290011428>
- Eberle, M. A., Grasset, O., & Sotin, C. (2002). A numerical study of the interaction between the mantle wedge, subducting slab, and overriding plate. *Physics of the Earth and Planetary Interiors*, *134*(3–4), 191–202. [https://doi.org/10.1016/S0031-9201\(02\)00157-7](https://doi.org/10.1016/S0031-9201(02)00157-7)
- Goes, S., Agrusta, R., Hunen, J. V., & Garel, F. (2017). Subduction-transition zone interaction: A review. *Geosphere*, *13*(3), 1–21. <https://doi.org/10.1130/GES01476.1>
- Hirose, K., Takafuji, N., Sata, N., & Ohishi, Y. (2005). Phase transition and density of subducted MORB crust in the lower mantle. *Earth and Planetary Science Letters*, *237*(1–2), 239–251. <https://doi.org/10.1016/j.epsl.2005.06.035>
- Hirschmann, M., & Kohlstedt, D. (2012). Water in Earth's mantle. *Physics Today*, *65*(3), 40–45. <https://doi.org/10.1063/pt.3.1476>
- Hofmeister, A. M. (1999). Mantle values of thermal conductivity and the geotherm from phonon lifetimes. *Science (New York, N.Y.)*, *283*(March), 1699–1707. <https://doi.org/10.1126/science.283.5408.1699>

- Hsieh, W., Ishii, T., Chao, K., Tsuchiya, J., Deschamps, F., & Ohtani, E. (2020). Spin transition of iron in δ -(Al,Fe)OOH induces thermal anomalies in Earth's lower mantle. *Geophysical Research Letters*, 47(4), e2020GL087036. <https://doi.org/10.1029/2020GL087036>
- Hsieh, W.-P., Chang, Y. Y., Tsao, Y. C., Lin, C. H., & Vilella, K. (2024). Exceptionally low thermal conduction of basaltic glasses and implications for the thermo-chemical evolution of the Earth's primitive magma ocean. *Journal of Geophysical Research: Solid Earth*, 129(2), e2023JB027722. <https://doi.org/10.1029/2023JB027722>
- Hsieh, W.-P., Chen, B., Li, J., Keblinski, P., & Cahill, D. G. (2009). Pressure tuning of the thermal conductivity of the layered muscovite crystal. *Physical Review B*, 80(18), 180302. <https://doi.org/10.1103/PhysRevB.80.180302>
- Hsieh, W.-P., Deschamps, F., Okuchi, T., & Lin, J.-F. (2017). Reduced lattice thermal conductivity of Fe-bearing bridgmanite in Earth's deep mantle. *Journal of Geophysical Research: Solid Earth*, 122(7), 4900–4917. <https://doi.org/10.1002/2017jb014339>
- Hsieh, W.-P., Deschamps, F., Okuchi, T., & Lin, J.-F. (2018). Effects of iron on the lattice thermal conductivity of Earth's deep mantle and implications for mantle dynamics. *Proceedings of the National Academy of Sciences of the United States of America*, 115(16), 4099–4104. <https://doi.org/10.1073/pnas.1718557115>
- Hsieh, W.-P., Deschamps, F., Tsao, Y.-C., Yoshino, T., & Lin, J.-F. (2024). A thermally conductive Martian core and implications for its dynamo cessation. *Science Advances*, 10(12), eadk1087. <https://doi.org/10.1126/sciadv.adk1087>
- Hsieh, W.-P., Ishii, T., Deschamps, F., Tsao, Y.-C., Chang, J.-W., & Criniti, G. (2024). Thermal conductivity of post-stishovite and CF phase. *Zenodo*. [Dataset] <https://zenodo.org/records/14002102>
- Hsieh, W.-P., Marzotto, E., Ishii, T., Dubrovinsky, L., Aslandukova, A. A., Criniti, G., et al. (2022). Low thermal conductivity of hydrous phase D leads to a self-preservation effect within a subducting slab. *Journal of Geophysical Research: Solid Earth*, 127(6), e2022JB024556. <https://doi.org/10.1029/2022JB024556>
- Hsieh, W.-P., Marzotto, E., Tsao, Y.-C., Okuchi, T., & Lin, J.-F. (2022). High thermal conductivity of stishovite promotes rapid warming of a sinking slab in Earth's mantle. *Earth and Planetary Science Letters*, 584, 117477. <https://doi.org/10.1016/j.epsl.2022.117477>
- Hsieh, W.-P., Tsao, Y. C., & Lin, C. H. (2022). Thermal conductivity of helium and argon at high pressure and high temperature. *Materials*, 15(19), 6681. <https://doi.org/10.3390/ma15196681>
- Hung, Y.-P. G., Tsao, Y.-C., Lin, C.-H., & Hsieh, W.-P. (2024). Thermal conductivity of aluminous garnets in Earth's deep interior. *American Mineralogist*, 109(3), 482–487. <https://doi.org/10.2138/am-2023-8953>
- Ishii, T., Chanyshv, A., & Katsura, T. (2022). A new approach determining a phase transition boundary strictly following a definition of phase equilibrium: An example of the post-spinel transition in Mg₂SiO₄ system. *Minerals*, 12(7), 820. <https://doi.org/10.3390/min12070820>
- Ishii, T., Criniti, G., Ohtani, E., Purevjav, N., Fei, H., Katsura, T., & Mao, H. k. (2022). Superhydrous aluminous silica phases as major water hosts in high-temperature lower mantle. *PNAS*, 119(44). <https://doi.org/10.1073/pnas>
- Ishii, T., Criniti, G., Wang, X., Glazyrin, K., & Ballaran, T. B. (2022). Synthesis and structural analysis of CaFe₂O₄-type single crystals in the NaAlSiO₄-MgAl₂O₄-Fe₃O₄ system. *American Mineralogist*, 108(1), 217–221. <https://doi.org/10.2138/am-2022-8748>
- Ishii, T., Frost, D. J., Kim, E. J., Chanyshv, A., Nishida, K., Wang, B., et al. (2023). Buoyancy of slabs and plumes enhanced by curved post-garnet phase boundary. *Nature Geoscience*, 16(9), 828–832. <https://doi.org/10.1038/s41561-023-01244-w>
- Ishii, T., Kojitani, H., & Akaogi, M. (2019). Phase relations of harzburgite and MORB up to the uppermost lower mantle conditions: Precise comparison with pyrolite by multisample cell high-pressure experiments with implication to dynamics of subducted slabs. *Journal of Geophysical Research: Solid Earth*, 124(4), 3491–3507. <https://doi.org/10.1029/2018JB016749>
- Ishii, T., Miyajima, N., Criniti, G., Hu, Q., Glazyrin, K., & Katsura, T. (2022). High pressure-temperature phase relations of basaltic crust up to mid-mantle conditions. *Earth and Planetary Science Letters*, 584, 117472. <https://doi.org/10.1016/j.epsl.2022.117472>
- Kaminsky, F. (2017). *The Earth's lower mantle-composition and structure*. Springer.
- Katsura, T., & Ito, E. (1989). The system Mg₂SiO₄-Fe₂SiO₄ at high pressures and temperatures: precise determination of stabilities of olivine, modified spinel, and spinel. *Journal of Geophysical Research*, 94(89), 15663–15670. <https://doi.org/10.1029/jb094i11p15663>
- Katsura, T., Yoneda, A., Yamazaki, D., Yoshino, T., Ito, E., Suetsugu, D., et al. (2010). Adiabatic temperature profile in the mantle. *Physics of the Earth and Planetary Interiors*, 183(1–2), 212–218. <https://doi.org/10.1016/j.pepi.2010.07.001>
- Kim, D., Jung, H., & Lee, J. (2023). Impact of chlorite dehydration on intermediate-depth earthquakes in subducting slabs. *Communications Earth and Environment*, 4(1), 491. <https://doi.org/10.1038/s43247-023-01133-5>
- Lakshatnov, D. L., Sinogeikin, S. V., Litasov, K. D., Prakupenka, V. B., Hellwig, H., Wang, J., et al. (2007). The post-stishovite phase transition in hydrous alumina-bearing SiO₂ in the lower mantle of the earth. *Proceedings of the National Academy of Sciences of the United States of America*, 104(34), 13588–13590. <https://doi.org/10.1073/pnas.0706113104>
- Li, Y., Deschamps, F., Yang, J., Chen, L., Zhao, L., & Tackley, P. J. (2019). Effects of the compositional viscosity ratio on the long-term evolution of thermochemical reservoirs in the deep mantle. *Geophysical Research Letters*, 46(16), 9591–9601. <https://doi.org/10.1029/2019GL083668>
- Lin, Y., Hu, Q., Meng, Y., Walter, M., & Mao, H. K. (2020). Evidence for the stability of ultrahydrous stishovite in Earth's lower mantle. *Proceedings of the National Academy of Sciences of the United States of America*, 117(1), 184–189. <https://doi.org/10.1073/pnas.1914295117>
- Lin, Y., Hu, Q., Walter, M. J., Yang, J., Meng, Y., Feng, X., et al. (2022). Hydrous SiO₂ in subducted oceanic crust and H₂O transport to the core-mantle boundary. *Earth and Planetary Science Letters*, 594, 117708. <https://doi.org/10.1016/j.epsl.2022.117708>
- Litasov, K., Ohtani, E., Sano, A., Suzuki, A., & Funakoshi, K. (2005). In situ X-ray diffraction study of post-spinel transformation in a peridotite mantle: Implication for the 660-km discontinuity. *Earth and Planet. Science LetterTh*, 238(3–4), 311–328. <https://doi.org/10.1029/2003JB002446>
- Litasov, K. D., Kagi, H., Shatskiy, A., Ohtani, E., Lakshatnov, D. L., Bass, J. D., & Ito, E. (2007). High hydrogen solubility in Al-rich stishovite and water transport in the lower mantle. *Earth and Planetary Science Letters*, 262(3–4), 620–634. <https://doi.org/10.1016/j.epsl.2007.08.015>
- Marzotto, E., Hsieh, W. P., Ishii, T., Chao, K. H., Golabek, G., Thielmann, M., & Ohtani, E. (2020). Effect of water on lattice thermal conductivity of ringwoodite and its implications for the thermal evolution of descending slabs. *Geophysical Research Letters*, 47(13), e2020GL087607. <https://doi.org/10.1029/2020GL087607>
- Meier, T., Trybel, F., Khandarkhaeva, S., Laniel, D., Ishii, T., Aslandukova, A., et al. (2022). Structural independence of hydrogen-bond symmetrisation dynamics at extreme pressure conditions. *Nature Communications*, 13(1), 3042. <https://doi.org/10.1038/s41467-022-30662-4>
- Muir, J. M. R., & Brodholt, J. P. (2018). Water distribution in the lower mantle: Implications for hydrolytic weakening. *Earth and Planetary Science Letters*, 484, 363–369. <https://doi.org/10.1016/j.epsl.2017.11.051>
- Nisr, C., Chen, H., Leinenweber, K., Chizmeshya, A., Prakupenka, V. B., Prescher, C., et al. (2020). Large H₂O solubility in dense silica and its implications for the interiors of water-rich planets. *Proceedings of the National Academy of Sciences*, 117(18), 9747–9754. <https://doi.org/10.1073/pnas.1917448117>
- Ohtani, E. (2020). The role of water in Earth's mantle. *National Science Review*, 7(1), 224–232. <https://doi.org/10.1093/nsr/nwz071>
- Ohtani, E., & Ishii, T. (2024). Role of water in dynamics of slabs and surrounding mantle. *Progress in Earth and Planetary Science*, 11(1), 1–20. <https://doi.org/10.1186/s40645-024-00670-7>

- Ohtani, E., Mizobata, H., & Yurimoto, H. (2000). Stability of dense hydrous magnesium silicate phases in the systems Mg_2SiO_4 - H_2O and $MgSiO_3$ - H_2O at pressures up to 27 GPa. *Physics and Chemistry of Minerals*, 27(8), 533–544. <https://doi.org/10.1007/s002690000097>
- Ono, A., Akaogi, M., Kojitani, H., Yamashita, K., & Kobayashi, M. (2009). High-pressure phase relations and thermodynamic properties of hexagonal aluminous phase and calcium-ferrite phase in the systems $NaAlSiO_4$ - $MgAl_2O_4$ and $CaAl_2O_4$ - $MgAl_2O_4$. *Physics of the Earth and Planetary Interiors*, 174(1–4), 39–49. <https://doi.org/10.1016/j.pepi.2008.07.028>
- Ono, S., Ito, E., & Katsura, T. (2001). Mineralogy of subducted basaltic crust (MORB) from 25 to 37 GPa, and chemical heterogeneity of the lower mantle. *Earth and Planetary Science Letters*, 190(1–2), 57–63. [https://doi.org/10.1016/S0012-821X\(01\)00375-2](https://doi.org/10.1016/S0012-821X(01)00375-2)
- Paterson, M. S. (1982). The determination of hydroxyl by infrared adsorption in quartz, silicate glasses and similar materials. *Bulletin de Mineralogie*, 105(1), 20–29. <https://doi.org/10.3406/bulmi.1982.7582>
- Peslier, A. H., Schönbacher, M., Busemann, H., & Karato, S. I. (2017). Water in the Earth's interior: Distribution and origin. *Space Science Reviews*, 212(1–2), 743–810. <https://doi.org/10.1007/s11214-017-0387-z>
- Purejav, N., Fei, H., Ishii, T., Criniti, G., Lin, Y., Mao, H. K., & Katsura, T. (2024). Temperature dependence of H_2O solubility in Al-free stishovite. *Geophysical Research Letters*, 51(3). <https://doi.org/10.1029/2023GL104029>
- Ricolleau, A., Perrillat, J. P., Fiquet, G., Daniel, I., Matas, J., Addad, A., et al. (2010). Phase relations and equation of state of a natural MORB: Implications for the density profile of subducted oceanic crust in the Earth's lower mantle. *Journal of Geophysical Research*, 115(B8), B08202. <https://doi.org/10.1029/2009JB006709>
- Takaichi, G., Nishihara, Y., Matsukage, K. N., Nishi, M., Higo, Y., Tange, Y., et al. (2024). Limited stability of hydrous SiO_2 stishovite in the deep mantle. *Earth and Planetary Science Letters*, 640, 118790. <https://doi.org/10.1016/j.epsl.2024.118790>
- Tang, X., Ntam, M. C., Dong, J., Rainey, E. S. G., & Kavner, A. (2014). The thermal conductivity of Earth's lower mantle Xiaoli. *Geophysical Research Letters*, 41(8), 2746–2752. <https://doi.org/10.1002/2014GL059385>. Received
- Tsutsumi, Y., Sakamoto, N., Hirose, K., Tagawa, S., Umemoto, K., Ohishi, Y., & Yurimoto, H. (2024). Retention of water in subducted slabs under core–mantle boundary conditions. *Nature Geoscience*, 17(7), 697–704. <https://doi.org/10.1038/s41561-024-01464-8>
- Tutti, F., Dubrovinsky, L. S., & Saxena, S. K. (2000). High pressure phase transformation of jadeite and stability of $NaAlSiO_4$ with calcium-ferrite type structure in the lower mantle conditions. *Geophysical Research Letters*, 27(14), 2025–2028. <https://doi.org/10.1029/2000GL008496>
- Wang, W., Xu, Y., Sun, D., Ni, S., Wentzcovitch, R., & Wu, Z. (2020). Velocity and density characteristics of subducted oceanic crust and the origin of lower-mantle heterogeneities. *Nature Communications*, 11(1), 64. <https://doi.org/10.1038/s41467-019-13720-2>
- Wei, S. S., Wiens, D. A., van Keken, P. E., & Cai, C. (2017). Slab temperature controls on the Tonga double seismic zone and slab mantle dehydration. *Science Advances*, 3(1), e1601755. <https://doi.org/10.1126/sciadv.1601755>
- Wu, Y., Qin, F., Wu, X., Huang, H., McCammon, C. A., Yoshino, T., et al. (2017). Spin transition of ferric iron in the calcium-ferrite type aluminous phase. *Journal of Geophysical Research: Solid Earth*, 122(8), 5935–5944. <https://doi.org/10.1002/2017JB014095>
- Xu, Y., Shankland, T. J., Linhardt, S., Rubie, D. C., Langenhorst, F., & Klasinski, K. (2004). Thermal diffusivity and conductivity of olivine, wadsleyite and ringwoodite to 20 GPa and 1373 K. *Physics of the Earth and Planetary Interiors*, 143–144, 321–336. <https://doi.org/10.1016/j.pepi.2004.03.005>
- Yang, R., & Wu, Z. (2014). Elastic properties of stishovite and the $CaCl_2$ -type silica at the mantle temperature and pressure: An ab initio investigation. *Earth and Planetary Science Letters*, 404, 14–21. <https://doi.org/10.1016/j.epsl.2014.07.020>
- Yin, K., Zhou, H. Q., & Lu, X. C. (2016). Thermodynamic properties of calcium ferrite-type $MgAl_2O_4$: A first principles study. *Science China Earth Sciences*, 59(4), 831–839. <https://doi.org/10.1007/s11430-015-5237-9>
- Zhang, Y., Fu, S., Karato, S. I., Okuchi, T., Chariton, S., Prakapenka, V. B., & Lin, J. F. (2022). Elasticity of hydrated Al-bearing stishovite and post-stishovite: Implications for understanding regional seismic VS anomalies along subducting slabs in the lower mantle. *Journal of Geophysical Research: Solid Earth*, 127(4). <https://doi.org/10.1029/2021JB023170>
- Zhang, Y., Yoshino, T., Yoneda, A., & Osako, M. (2019). Effect of iron content on thermal conductivity of olivine with implications for cooling history of rocky planets. *Earth and Planetary Science Letters*, 519, 109–119. <https://doi.org/10.1016/j.epsl.2019.04.048>
- Zhang, Z., Zhang, D., Onga, K., Hasegawa, A., Ohta, K., Hirose, K., & Wentzcovitch, R. M. (2021). Thermal conductivity of $CaSiO_3$ perovskite at lower mantle conditions. *Physical Review B: Condensed Matter*, 104(18), 184101. <https://doi.org/10.1103/PhysRevB.104.184101>
- Zhao, M., Zhou, H., Yin, K., Sun, Y., Liu, X., Xu, S., & Lu, X. (2018). Thermoelastic properties of aluminous phases in MORB from first-principle calculation: Implications for Earth's lower mantle. *Journal of Geophysical Research: Solid Earth*, 123(12), 10583–10596. <https://doi.org/10.1029/2018JB016491>
- Zheng, X., Cahill, D. G., Krasnochtchekov, P., Averback, R. S., & Zhao, J. C. (2007). High-throughput thermal conductivity measurements of nickel solid solutions and the applicability of the Wiedemann-Franz law. *Acta Materialia*, 55(15), 5177–5185. <https://doi.org/10.1016/j.actamat.2007.05.037>
- Zhou, Y., Dong, Z.-Y., Hsieh, W.-P., Goncharov, A. F., & Chen, X.-J. (2022). Thermal conductivity of materials under pressure. *Nature Reviews Physics*, 4(5), 319–335. <https://doi.org/10.1038/s42254-022-00423-9>